Mercury intrusion porosimetry as a quantitative tool for the shape estimation of supraparticles generated via spray-drying

*Ahammed Suhail Odungat[1, †], Adil Amin[1, †], Moritz Loewenich[2], Blaž Toplak[1], Mena-Alexander Kräenbring[1], Mohaned Hammad[1], Hartmut Wiggers[2,3], Doris Segets[1,3], Fatih Özcan[1, 3, *]*

[1]Institute for Energy and Materials Processes – Particle Science and Technology (EMPI – PST), University of Duisburg-Essen (UDE), Germany

[2]Institute for Energy and Materials Processes − Reactive Fluids (EMPI – RF), University of Duisburg-Essen (UDE), Germany

[3]Center for Nanointegration Duisburg-Essen (CENIDE), University of Duisburg-Essen (UDE), Germany

Corresponding Author

[*]Email: fatih.oezcan@uni-due.de

[†]*These authors contributed equally to this work*

Keywords

Supraparticles, Shape, Mercury intrusion porosimetry, Silicon-carbon, Porosity, Lithium-ion battery anode

Abstract

Supraparticles are hierarchically structured assemblies of nanoparticles whose size and structural features such as shape, surface roughness, and porosity critically govern their functionality in applications such as energy storage and catalysis. While size and porosity can be measured reliably using established techniques, there is a lack of robust and statistically meaningful methods for assessing supraparticle shape. In this work, we present a novel methodology for estimating supraparticle shape based on mercury intrusion porosimetry (MIP). First, we were able to unravel that the characteristic two-stage intrusion profile of supraparticles corresponds to inter- and intra-supraparticle pores. Then, deconvolution of the MIP pore size distributions enabled separation of these contributions, while assignment of their physical origin was realized by comparison of the extracted intra-supraparticle peaks with the pore size distributions of constituent nanoparticles. By employing a design of experiment that enabled varying supraparticle size and shape independently, we established that the extent of bimodality in MIP pore size distributions is strongly correlated with supraparticle shape. Quantitative shape descriptors obtained from scanning electron microscope-based circularity measurements were compared with statistical metrics of bimodality (Ashman's D and peak separation) derived from deconvoluted distributions. A clear relationship emerged: supraparticles with higher circularity exhibited more pronounced bimodality, whereas irregular particles showed diminished or poorly resolved bimodal features. This work therefore introduces a statistically reliable approach for simultaneous evaluation of supraparticle porosity and shape, with direct implications for scale up, process optimization and quality control in industrial spray-drying processes.

1. Introduction

Supraparticles are hierarchically structured secondary particles assembled from smaller building blocks, such as nanoparticles. The supraparticles formed from nanoparticles exhibit collective properties that are distinct from, yet partially preserve, the intrinsic characteristics of their constituent nanoparticles [1–5]. For instance, supraparticles can retain catalytic activity while simultaneously offering enhanced pore structure and processability [6,7]. Owing to such unique features, supraparticles have attracted growing interest across diverse fields, including air and water purification [8,9], catalysis [10,11], and sustainable energy storage and conversion [12,13].

Supraparticles are also emerging as a promising approach to address the limitations of conventional nanomaterial-based electrodes in lithium-ion batteries (LIBs). Silicon is widely regarded as a next-generation anode material owing to its exceptionally high theoretical specific capacity [15]. However, its practical implementation is hindered by several challenges, including rapid capacity fading and low Coulombic efficiency, both arising from the substantial volume expansion during lithiation [16]. While nanostructured silicon offers improvements by reducing diffusion lengths, improving fracture resistance and enhancing electrochemical performance, the direct use of nanoparticles suffers from drawbacks such as low packing density and high interparticle resistance [17–21]. The use of supraparticles made from Si-based nanoparticles has helped to overcome most of the mentioned issues [22–25]. Amin et al. developed supraparticles composed of silicon–carbon (Si/C) composite nanoparticles via a scalable, single-step spray-drying process. This strategy, yielding supraparticles with improved coating density, slurry processability, and scalability for commercial manufacturing, alongside enhanced cycling stability, leverages the advantages of nanoscale silicon while mitigating its intrinsic drawbacks [6].

In any application, the performance and processability of supraparticles are critically influenced by their size and structural characteristics, particularly shape, surface roughness, and porosity [26,27]. In the context of LIB anodes, these features dictate key factors such as the extent of electrolyte–electrode interfacial contact, lithium-ion diffusion throughout the active material, and the ability to accommodate the substantial volume expansion that occurs during lithiation [7]. The size and structural features of supraparticles can be tuned by parameters including the properties of the nanoparticle

building blocks, the supraparticle formation technique, and the specific process conditions employed [7]. Reliable, robust, and statistically significant methods exist for size determination using analytical centrifugation (AC) or dynamic light scattering and for porosity characterization using mercury intrusion or nitrogen adsorption porosimetry. However, comparable approaches for assessing supraparticle shape at the ensemble level remain underdeveloped. Conventional imaging techniques, such as scanning electron microscopy (SEM) and computed tomography, provide high-resolution structural information but are inherently limited by low throughput and small sampling volumes, which compromises their statistical reliability when assessing bulk powder production. Imaging-based approaches for statistically supported shape analysis are evolving, such as combined laser diffraction and dynamic image analysis systems that couple ensemble size measurements with optical shape descriptors. But reliable shape assessment of particles in the lower micrometer range at the ensemble level remains a significant challenge. These limitations underscore the need for alternative characterization strategies that enable scalable, reproducible, and statistically robust shape analysis of supraparticles.

In this study, we present a novel methodology to estimate the shape of Si/C supraparticles using mercury intrusion porosimetry (MIP). MIP is an established analytical technique commonly used to characterize the pore structure of materials. During the analysis, mercury, which is a non-wetting liquid, is forced into the pores of a sample under controlled external pressure. The relationship between the applied pressure and the volume of mercury intruded is then used to calculate various pore properties, including pore size distribution, total pore volume, and porosity. Our analysis approach utilizes MIP data to infer shape of supraparticle ensembles while simultaneously providing porosity information, with statistically significant reliability. The method has been rigorously validated through a design of experiments framework, in which the size and shape of supraparticles were systematically varied by tuning feed nanoparticle sizes and spray-drying parameters. The developed methodology offers a rapid, scalable, and quantitative alternative for supraparticle shape characterization, with significant implications for the optimization of electrode architectures in high-performance LIBs and beyond.

We selected Si/C supraparticles as the primary system for establishing our methodology. This choice was motivated by two considerations: first, their high

relevance as potential LIB anode materials, and second, the intrinsic characteristics of their constituent Si/C nanoparticles. The Si/C nanoparticles, synthesized in a hot-wall reactor from monosilane and ethylene, exhibit a broad distribution of average primary particle sizes ranging from 60 nm to 190 nm and partially sinter into aggregates with varying shapes and dimensions. We hypothesized that, if our method proves to be effective for supraparticles assembled from such inherently heterogeneous nanoparticles, it can be applied to a wide range of materials produced from other types of nanoparticles via spray-drying.

2. Experimental section

2.1. Preparation of Si/C supraparticles

Si/C nanoparticles were synthesized via spray-flame synthesis following the procedure reported by Orthner et al [28]. These nanoparticles were subsequently assembled into supraparticles using a scalable, one-step, non-reactive spray-drying protocol developed by Amin et al. [6]. The spray-drying dispersion consisted of Si/C nanoparticles (3 wt%), polyacrylic acid (1 wt%, 25 wt% in water, Thermo Scientific) as an agglomerate stabilizer, and ultrapure water (18.2 MΩ·cm, Milli-Q). The mixture was premixed for 24 h at 500 rpm using a magnetic stirrer prior to spray-drying. Different supraparticle sizes were obtained by varying the gas-to-liquid ratio (GLR), a key parameter in the spray-drying process. An increase in GLR reduces the droplet size during atomization, resulting in smaller supraparticles [29]. Throughout synthesis, the following conditions were held constant: liquid flow rate at 0.3 L/h, drying gas flow rate at 35,000 L/h, and drying temperature at 150 °C. Nitrogen was used as the spraying gas, with flow rates of 439, 667, and 1052 L/h corresponding to GLRs of 1.5k, 2.2k, and 3.5k, respectively. Spray-drying was performed using a Büchi spray-dryer (B290, Büchi GmbH) at ambient pressure.

2.2. Characterization of supraparticles

The size of the supraparticles (size of the sedimentation-equivalent, dense sphere) was determined using an AC (LUMiSizer 651-44, LUM GmbH) by dispersing the samples in Milli-Q water. The AC analysis was performed using a polycarbonate cuvette with a 2 mm optical path length. Morphological analysis was carried out using two different SEMs based on their availability to the project, a Thermo Fisher Philips XL20 and a Helios NanoLab 600i. Pore characteristics of both nanoparticles and

supraparticles were investigated using a MIP device (Anton Paar Porosimeter 60). For each measurement, 350 mg of sample was loaded as lose powder into the measuring cell, and the properties were analyzed separately in the low-pressure and high-pressure units. Prior to all measurements in the low-pressure unit, the system was evacuated to 9.66×10^{-4} psi before filling with mercury. In the high-pressure unit, the applied pressure was gradually increased from 20 psi to 60,000 psi. The volume of mercury intruded was normalized to the sample weight to obtain pore properties.

3. Results and discussion

As explained in the introduction, the aim of this work is to establish a methodology for supraparticle shape estimation at the ensemble level, closing the gap left by conventional techniques that fail to provide statistically meaningful information on several structural properties. For this, we propose a methodology in which two of the key structural features, such as pore characteristics and shape, can be obtained from a single characterization technique, MIP. In the following sections, we first describe the working principle of MIP and the mechanism of mercury intrusion in the context of supraparticles. We then present the developed approach for shape estimation and validate it through a systematic design of experiments (DoE): (i) supraparticles of different sizes synthesized from the same batch of nanoparticles, and (ii) supraparticles of comparable size but differing shapes obtained by varying the average size of the feed nanoparticles.

The structural properties of supraparticles investigated in this study are illustrated in Figure 1a. The figure includes an SEM image of a representative supraparticle, highlighting key structural features. In this context, shape refers to the overall geometry of the supraparticle, specifically the degree to which it is spherical or non-spherical. Surface properties, particularly surface roughness, are also considered in this work as this parameter reflects the smoothness of the supraparticle surface and the extent of surface defects. A further structural property of interest is porosity, which captures the internal pore architecture of the supraparticles. This is visualized in the focused ion beam (FIB)-SEM cross-sectional image shown in the inset of Figure 1a.

3.1 Mercury intrusion porosimetry of supraparticles

MIP has traditionally been employed to characterize the pore properties of a wide range of porous materials [32–37]. The technique operates by forcefully intruding

mercury, which is a non-wetting liquid, into the pores of a sample under controlled external pressure, while recording the corresponding volume of mercury intruded. The inverse relationship between applied pressure and pore diameter, described by Washburn's equation (Equation 1), is then used to estimate pore sizes and construct the pore size distribution [33,37].

$$Pore\ diameter = \frac{2 \times \gamma \times cos\theta}{P} \qquad \text{(Equation 1)}$$

Where P is the applied pressure, θ is the contact angle and γ is the surface tension of mercury. For a typical supraparticle as shown in Figure 1a, a characteristic two-stage mercury intrusion process can be expected: (i) intrusion into the voids between the supraparticles (inter-supraparticle pores), and (ii) intrusion into the internal pores within the supraparticles (intra-supraparticle pores). A schematic representation of this two-stage intrusion is shown in Figure 1b, where (1) and (2) denote inter- and intra-supraparticle intrusion, respectively. The intrusion into inter-supraparticle pores typically occurs at lower external pressures, while intra-supraparticle mercury intrusion requires higher external pressures because of the small pore diameter.

The anticipated two-stage intrusion behavior was clearly reflected in the MIP data. Figure 1c shows the cumulative mercury intrusion volume of supraparticles (normalized to sample weight) as a function of applied external pressure. The intrusion profile exhibits an initial increase at lower pressures, followed by a plateau, and then a second increase beginning at approximately 1000 psi. This behavior corresponds to the two-stage intrusion described above: the volume increase at lower pressures, denoted as (1) in the figure, is associated with inter-supraparticle pores, while the increase at higher pressures corresponds to intra-supraparticle pores, denoted as (2). From the intrusion profile, the pore size distribution was derived, which is a characteristic bimodal distribution (Figure 1d). The two peaks, centered at 0.26 μm and 0.85 μm, are expected to correspond to intra- and inter-supraparticle pores, respectively. The pore characteristics were further compared across supraparticles of varying sizes and structures to investigate the influence of synthesis conditions on their hierarchical porosity.

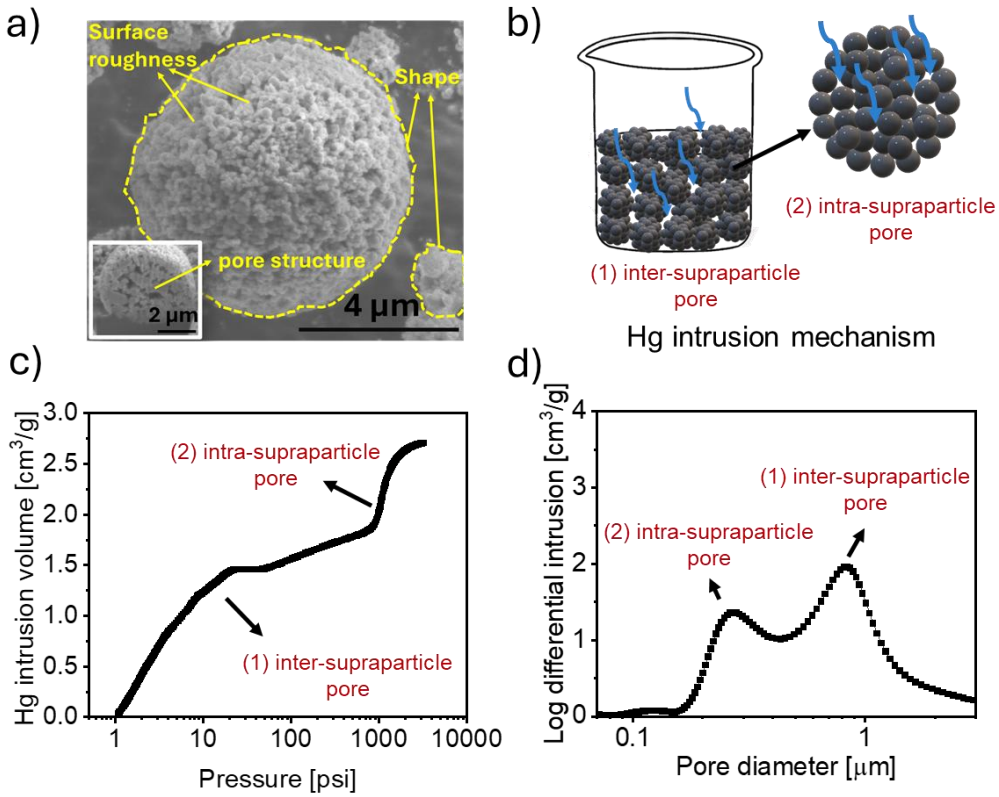

***Figure 1**: Supraparticle structural properties and MIP analysis. (a) SEM image of a spherical supraparticle illustrating key structural properties with the inset showing the FIB cut through the supraparticle; (b) schematic representation of the two-stage mercury intrusion process; (c) cumulatively intruded volume of mercury with increasing external pressure; (d) pore size distribution generated from the MIP intrusion data.*

3.2 Design of experiment

3.2.1 Supraparticles of different sizes synthesized from nanoparticles of same size

Si/C supraparticles of varying sizes were prepared from a single batch of nanoparticles with a mean primary particle size of 185 nm by adjusting the GLR during spray-drying. As demonstrated in our previous study, an increase in GLR reduces the droplet size during atomization, which in turn decreases the average size of the resulting supraparticles [7]. All other spray-drying conditions were kept constant except for the GLR, which varied from 1.5k, 2.2k, and 3.5k, respectively. The volume-based size distributions obtained by AC for supraparticles formed at different GLRs are shown in Figure 2a. The results clearly indicate a progressive shift of the size distribution toward smaller diameters with increasing GLR, confirming the expected trend. The median particle sizes $x_{50,3}$, calculated from the particle size distribution, for GLRs of 1.5k, 2.2k, and 3.5k were determined to be 5.0 µm, 3.3 µm, and 2.0 µm, respectively. Also, the

SEM images in Figure 2 b-d reveal that the supraparticles are becoming progressively irregular in shape as their median size decreases.

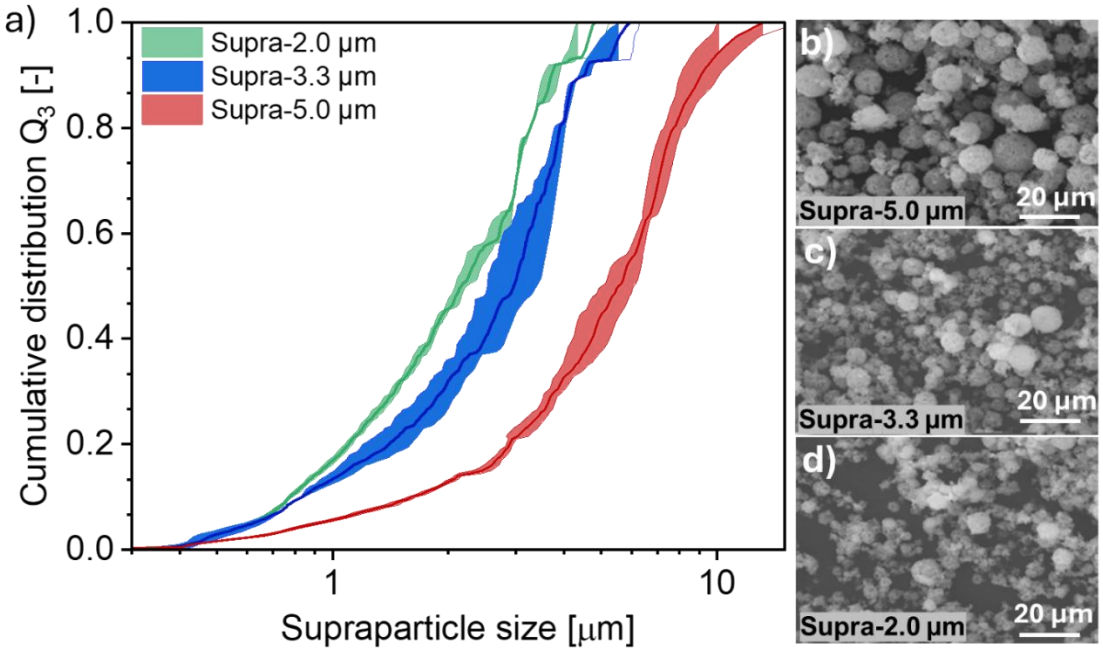

***Figure 2**: Particle size and shape analysis of supraparticles of different size formed from the same batch of nanoparticles. (a) Particle size distributions (sedimentation equivalent, dense sphere) from AC analysis. Reprinted (adapted) with permission from [7], Copyright 2025 American Chemical Society; (b), (c) and (d) are the SEM images of supraparticles of median sizes of 5.0, 3.3 and 2.0 µm, respectively.*

Further, MIP pore analysis was performed on all supraparticles to investigate how pore characteristics are influenced by variations in synthesis conditions. Figure 3 shows the pore size distributions of the supraparticles compared with that of the feed nanoparticles prior to supraparticle formation. The supraparticles exhibit bimodal pore size distributions, consistent with the presence of both inter- and intra-supraparticle pores as described in Section 3.1. In contrast, the feed nanoparticles display a unimodal distribution with a peak centered at 0.4 µm, indicating that only interparticle pores between nanoparticles are detected in this case. Any smaller pores within individual nanoparticles are below the resolution limit of the MIP technique. Notably, the lower-diameter peak of all supraparticles is well-aligned, centered at ~0.6 µm, confirming that the intra-supraparticle pores remain constant. This is in line with expectations as the same nanoparticle batch was used across all spray drying campaigns for supraparticle assembly. In contrast, the peak at larger diameters,

corresponding to inter-supraparticle pores, shows a pronounced variation. Specifically, the peak position shifts from 1.1 μm for supraparticles with a median size of 2.0 μm to 2.1 μm for supraparticles with a median size of 5.0 μm. This systematic shift reflects the change in inter-supraparticle spacing that accompanies increasing supraparticle size, resulting in larger inter-supraparticle pores.

Another key observation from the pore size distribution is that the degree of bimodality is not constant but decreases as the supraparticle size is reduced. While the shift in peak positions can be attributed to differences in supraparticle size, the change in bimodality appears to be associated with the supraparticle shape. As mentioned above, the supraparticles become progressively more irregular in shape as their size decreases. Supraparticles with a median size of 5.0 μm (supra-5.0) are largely spherical, whereas those with a median size of 2.0 μm (supra-2.0) display highly irregular shapes. For nearly spherical supraparticles, packing results in a clear separation between inter- and intra-supraparticle pores, producing a pronounced bimodal pore size distribution. In contrast, when supraparticles are highly irregular in geometry, with little to no defined shape, they can pack more tightly and randomly. This reduces the distinction between inter- and intra-supraparticle pores, which likely explains the diminished bimodality observed in the pore size distribution of supra-2.0. To validate the hypothesis that the bimodality of the MIP pore size distribution is influenced by the supraparticle shape, and to isolate this effect from that of supraparticle size, supraparticles of similar sizes but varying shapes were analyzed. The results are discussed in the subsequent section.

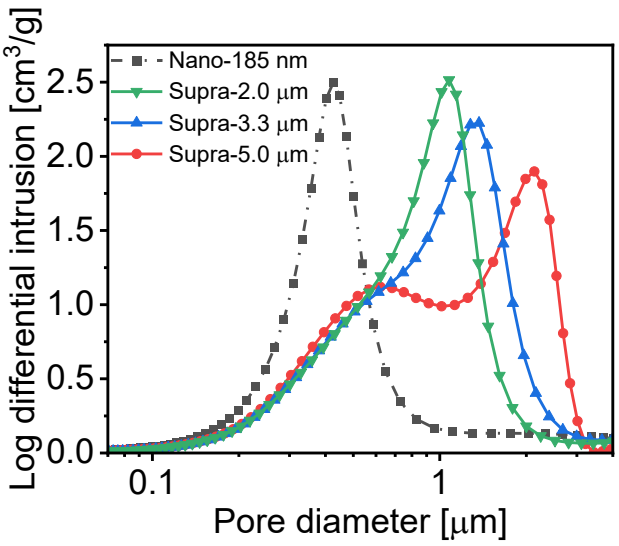

***Figure 3**: MIP pore size distributions of supra-5.0, supra-3.3, supra-2.0 and their constituent nanoparticle powder of average size 185 nm as determined from TEM images.*

3.2.2 Supraparticles of same size but different shape

So far, our results indicate that the bimodality of the MIP pore size distribution of supraparticles correlates with variations in supraparticle shape or size. At this stage, it cannot be conclusively attributed to shape alone. To disentangle these effects, we performed MIP measurements on supraparticles of same size but different shapes. These supraparticles were obtained by varying the mean size of the feed nanoparticles while keeping the spray-drying conditions constant. Nanoparticles with mean primary particle diameters of 60, 84, 115, and 185 nm were used as building blocks to form supraparticles designated as supra-A, supra-B, supra-C, and supra-D, respectively. The nanoparticle sizes were determined by averaging measurements from at least 300 primary nanoparticles imaged by TEM (Supplementary Figure S1). The sizes of the resulting supraparticles were then analyzed by AC, which confirmed that all supraparticles had comparable sizes with a median diameter of a sedimentation-equivalent, dense sphere of 2 µm (Supplementary Figure S2).

SEM images of the supraparticles were obtained to assess their shape and are shown in Figure 4a-d. Preliminary visual inspection reveals significant differences in shape and surface roughness among the samples. Supraparticles in the supra-A sample appear predominantly spherical, with smoother surfaces. In supra-B, most particles retain a generally spherical form, but noticeable surface defects are present. For supra-C, pronounced holes and ruptures are evident in many particles. In contrast, the

particles in supra-D are completely irregular in shape, lacking any discernible spherical structure. This irregularity may originate from two primary factors. The first is related to particle packing within the spray-dried droplet. Since all spray-drying parameters were kept constant, the droplet size remained unchanged across samples. Larger nanoparticles may not pack as efficiently within these droplets as smaller ones, leading to incomplete structural consolidation during drying. Consequently, droplets containing smaller nanoparticles preserve the spherical geometry of the atomized droplet, whereas those containing larger nanoparticles solidify into irregular, distorted shapes due to inefficient packing.

The second factor is the reduced mechanical stability of the spray-dried secondary particles as the size of the primary nanoparticles increases. Wang et al. demonstrated for silica supraparticles that the mechanical stability decreases with increasing nanoparticle size, primarily due to weaker interparticle interactions [38]. A similar mechanism may apply to the Si/C supraparticles studied here. As the size of the nanoparticles increases, the resulting secondary particles may lose structural integrity, causing them to fracture into smaller, loosely bound agglomerates, as observed in the SEM image of supra-D in Figure 4d. Hence, these aggregates do not fully conform to the definition of supraparticles. Therefore, in the following sections, the term supra-D refers to the agglomerated secondary particles obtained by spray-drying nanoparticles with a mean primary particle diameter of 185 nm. The observations suggest that, when spray-drying parameters are held constant, increasing the size of the feed Si/C nanoparticles yields secondary particles of comparable overall size but progressively more irregular shapes.

MIP measurements were performed on all nanoparticles and their corresponding spray-dried secondary particles. The pore size distributions of the nanoparticles prior to supraparticle assembly are shown in Figure 4e. In the case of all nanoparticles, a predominant single peak is observed, which systematically shifts toward larger pore diameters as the nanoparticle size increases. The peak centers are located at 0.19, 0.21, 0.29, and 0.40 µm for nanoparticles with mean sizes of 60, 84, 115, and 185 nm, respectively. This trend can be attributed to the increasing interparticle spacing. As the size of the nanoparticles increases, the voids left between particles in the packing become larger, thereby shifting the peak center toward higher pore diameters.

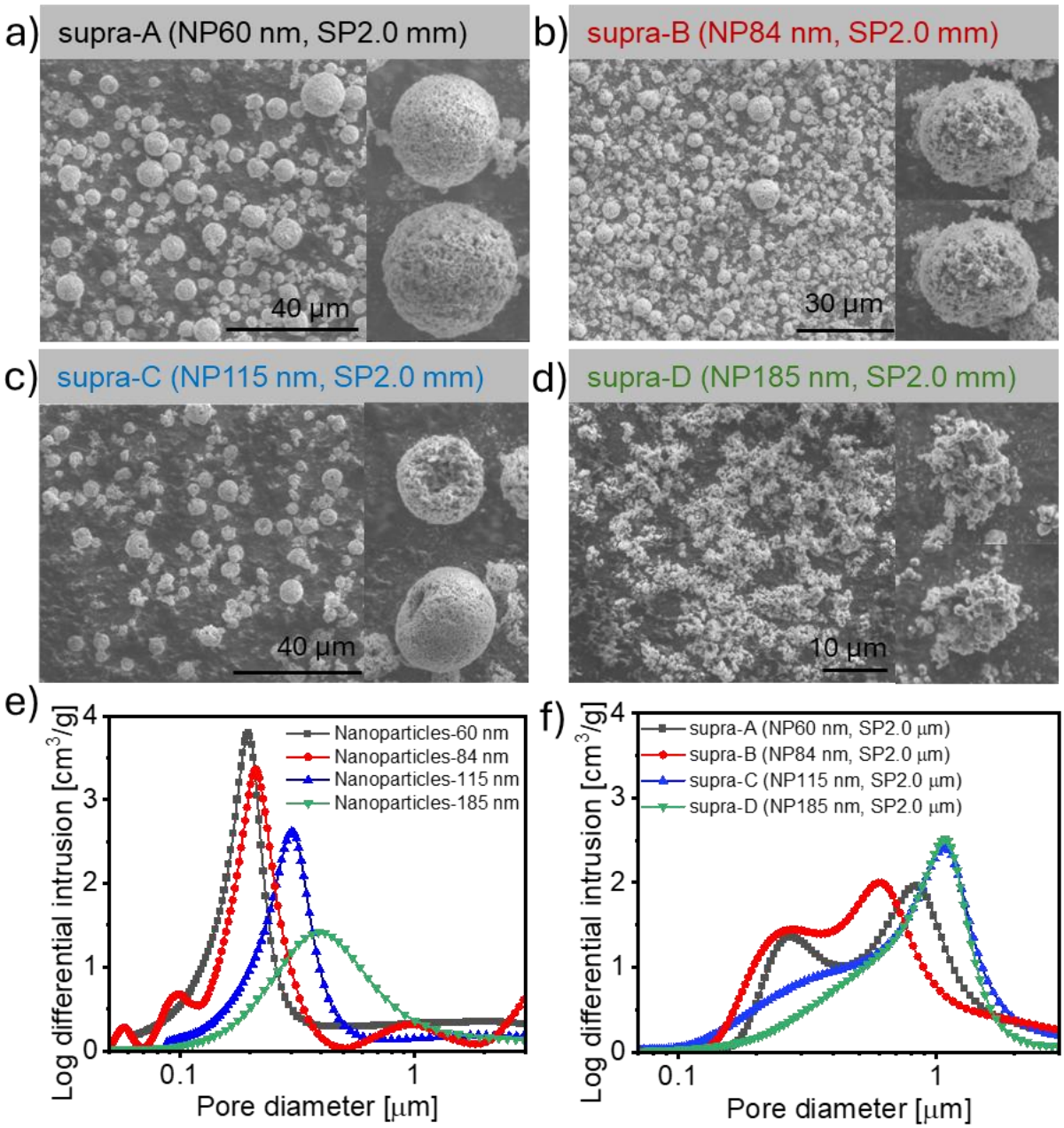

***Figure 4**: Shape and pore analysis of supraparticles formed from nanoparticles of different primary particle sizes at constant spray-drying parameters. (a), (b), (c) and (d) are the SEM images of supraparticles supra-A, supra-B, supra-C, and supra-D respectively; (e) MIP pore size distribution of the corresponding feed nanoparticles; (f) MIP pore size distribution of supraparticles.*

Figure 4f shows the MIP pore size distributions of spray-dried secondary particles formed from nanoparticles of different sizes. The first set of peaks, corresponding to intra-supraparticle porosity, lies between 0.24 µm and 0.49 µm, while the second set of peaks, corresponding to inter-supraparticle porosity, appears between 0.83 µm and 1.04 µm. As mentioned earlier, the only difference among these supraparticles is the

size of the constituent nanoparticles, which in turn affects their shape. This variation in shape is reflected in the pore size distributions. Although all distributions exhibit a bimodal character, the degree of bimodality varies systematically among the samples, decreasing in the order supra-A > supra-B > supra-C > supra-D. This trend is consistent with the observation made in Section 3.2a, which is, the bimodality of the pore size distribution increases as the supraparticles become more spherical. Since this set of supraparticles differs solely in the size of the feed nanoparticles and the resulting shape variation, these results conclusively demonstrate that the extent of bimodality in the MIP pore size distribution of Si/C supraparticles is governed by supraparticle shape.

Hence, we hypothesize that the shape of Si/C supraparticle powder samples can be qualitatively compared by examining their respective MIP pore size distributions, allowing us to infer which samples are more spherical and which are more irregular. In the following section, we aim to establish a quantitative correlation between the characteristics of the MIP pore size distribution and supraparticle shape.

3.3 Correlation between supraparticle shape and pore size distribution

In the previous sections, we demonstrated that the bimodality of the MIP pore size distribution is strongly dependent on supraparticle shape. To uncover this relationship quantitatively, both the shape of supraparticles and the degree of bimodality must be mathematically defined. In this section, these two properties are quantified and subsequently correlated to uncover the underlying structure-property relation and to provide a link between supraparticle shape and their corresponding MIP pore size distributions.

a) Supraparticle shape quantification

The shape of supraparticles can be quantified using sphericity as a parameter, which describes the degree to which an object approximates a perfect sphere. A higher sphericity value indicates a closer resemblance to a spherical geometry. However, this is not possible here as shape information was obtained from SEM images, which provide only two-dimensional projections. Therefore, a related metric, the circularity, was employed as a shortcut to approximate the supraparticle sphericity in two dimensions. The circularity provides a measure of how closely the 2D projection of a

supraparticle resembles a perfect circle. It is calculated by extracting the perimeter and area of each particle from SEM images according to:

$$circularity = \frac{4 \times \pi \times Area}{Perimeter^2} \qquad \text{(Equation 2)}$$

Shape information from 100 particles was extracted from SEM images for each supraparticle type, and the average circularity was calculated. The results are summarized in Figure 5, which compares the average circularities of supra-A, supra-B, supra-C, and supra-D. A decreasing trend is observed as the size of the feed nanoparticles increases. The average circularity values for supra-A, supra-B, supra-C, and supra-D are 0.90, 0.81, 0.80, and 0.32, respectively. While supra-A, supra-B, and supra-C exhibit similar values, a significant drop is observed for supra-D. This sharp decrease reflects the highly irregular geometry of supra-D, where no distinct spherical shape is formed, in contrast to supra-A to C, which retain a generally spherical structure with varying degrees of surface defects. These circularity values are in strong agreement with the visual observations from the SEM images described in Section 3.2. Thus, we conclude that the circularity provides a reliable quantitative descriptor of the supraparticle shape.

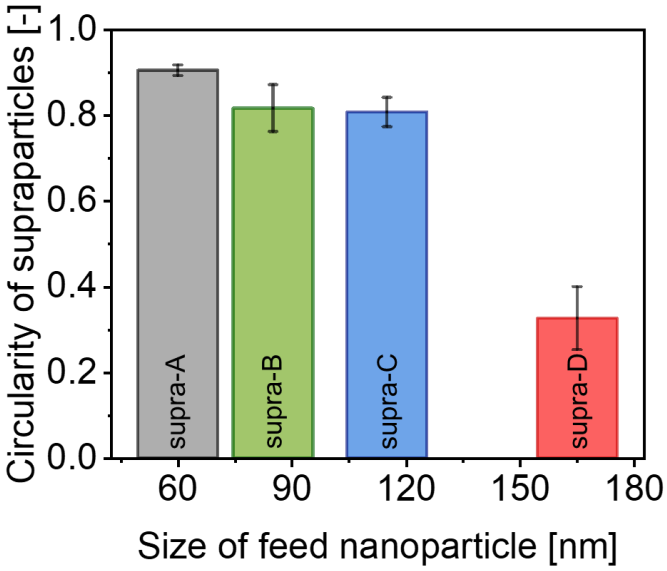

***Figure 5**: Average circularity of supraparticles: supra-A, supra-B, supra–C and supra-D.*

b) Extent of bimodality of the MIP pore size distribution

Prior to performing tests for bimodality of the supraparticle pore size distributions, the data were deconvoluted into their constituent components, corresponding to inter- and intra-supraparticle pores. All deconvolutions were performed under the assumption that the constituent components follow a Gaussian distribution, and by ensuring that the resultant cumulative peak fit maintains an R^2 value greater than 0.95. The resulting deconvoluted peaks were then used to calculate the mean values and standard deviations separately for each component. Figure 6 presents the deconvoluted pore size distributions of all the supraparticles. The larger peak, centered at higher diameters and shown in red, corresponds to the inter-supraparticle pores (Fit Peak 1), while the smaller peak, centered at lower diameters and shown in green, corresponds to the intra-supraparticle pores (Fit Peak 2). The mean pore diameters and standard deviations of Fit Peaks 1 and 2 are summarized in Supplementary Table T1.

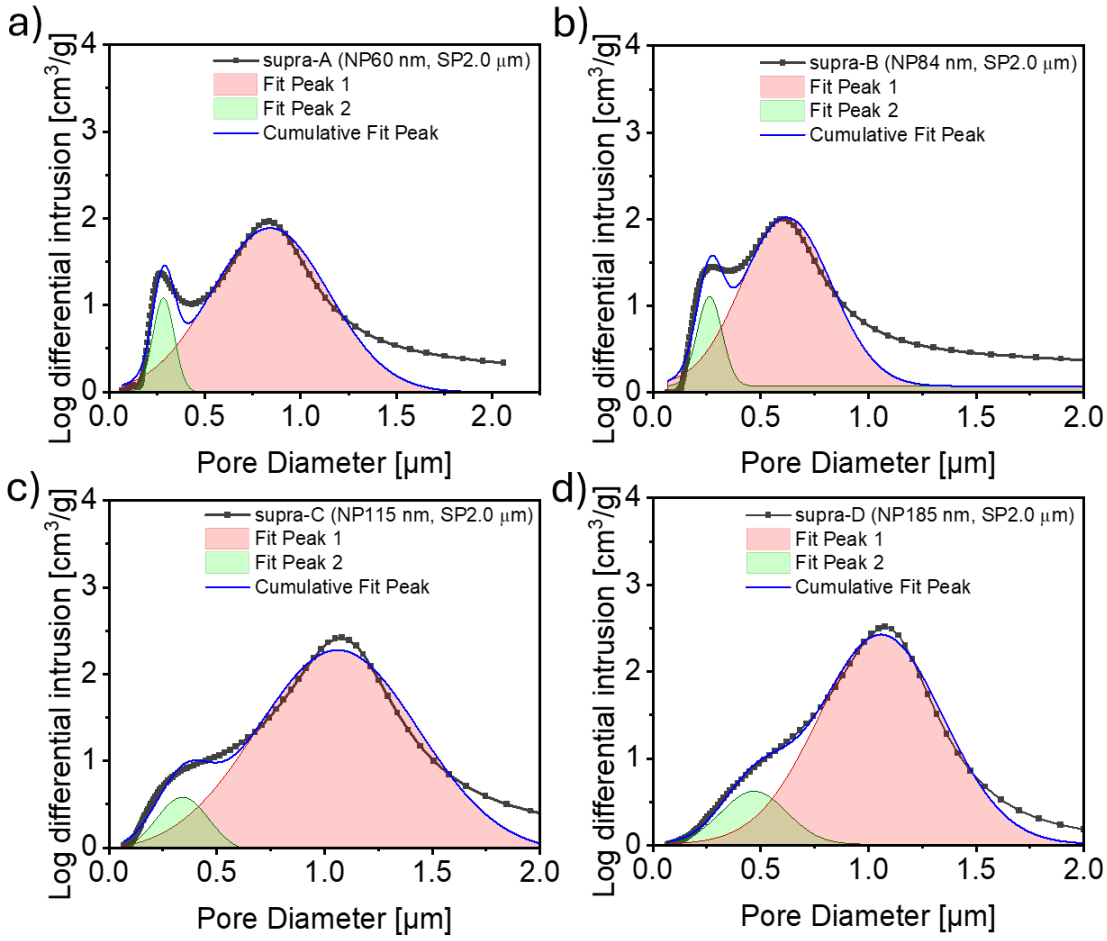

***Figure 6**: Peak deconvolutions performed on MIP pore size distributions of a) supra-A, b) supra-B, c) supra-C, and d) supra-D.*

The reliability of the peak deconvolution method was evaluated by comparing the intra-supraparticle pore peaks obtained from deconvoluted MIP pore size distributions with the MIP pore size distributions of the powders of the corresponding constituent nanoparticles. Figure 7 shows the pore size distributions of the nanoparticles alongside the extracted intra-supraparticle peaks of the corresponding supraparticles. An important observation is that the intra-supraparticle pore peaks fall within the same pore size regime as in case of the powders from their constituent nanoparticles. This is expected since intra-supraparticle pores essentially represent the voids between nanoparticles. Another important trend is that the shift in the peak centers with increasing nanoparticle size is preserved in the intra-supraparticle pores. Specifically, the average intra-supraparticle pore sizes follow the order supra-A ≈ supra-B > supra-C > supra-D, only slightly inconsistent with the sizes of their respective feed nanoparticles. In addition, the peak widths broaden from supra-A to supra-D, as reflected in the FWHM values of 0.13 μm and 0.37 μm, respectively. A similar broadening trend is observed for nanoparticle powders as well.

A notable difference between the MIP pore size distributions of nanoparticles and the extracted intra-supraparticle pore size distributions is a slight rightward shift of the latter toward larger pore diameters. This may be attributed to the enhanced structural rigidity of supraparticles. It should also be noted that MIP tends to underestimate pore sizes in softer materials due to the inherent sample compression during the measurement, an effect that can be more pronounced in loose nanoparticle powders than in consolidated supraparticles. Since supraparticles exhibit higher mechanical stability and structural rigidity, they are less susceptible to compression artifacts, resulting in slightly larger apparent intra-supraparticle pore sizes compared to their constituent nanoparticle powders [31,38]. The strong correspondence between the pore size distributions of nanoparticles and intra-supraparticle pores supports the validity of our peak deconvolutions. This, in turn, provides confidence in using the deconvoluted peaks for further calculations and analysis.

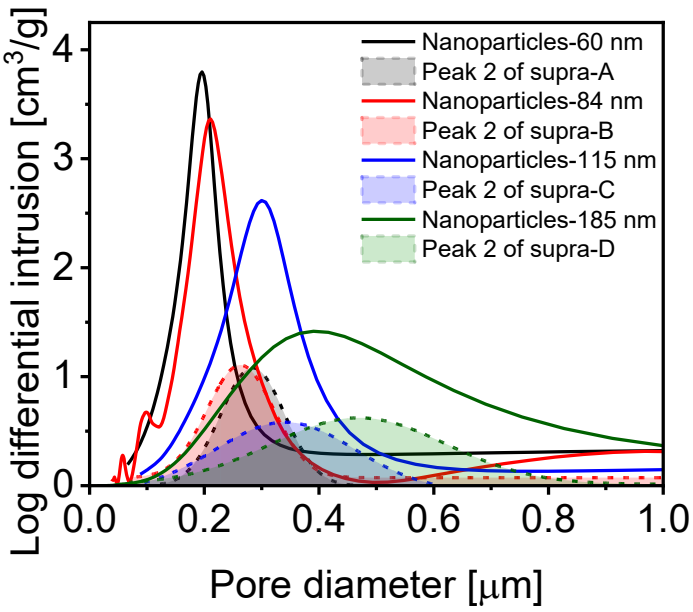

***Figure 7**: Comparison of the intra-supraparticle pore size distributions (Peak 2) with their corresponding pore size distributions of the nanoparticle powders.*

Having established a reliable deconvolution method for extracting intra- and inter-supraparticle pore information from the MIP pore size distributions, we next investigated the dependence of the MIP bimodality on supraparticle shape. For this, we evaluated the degree of bimodality in the supraparticle pore size distribution curves using two statistical measures, Ashman's D-value (D_A) and the bimodality peak separation value. These are the two commonly used statistical metrics that enables us to calculate the extent of bimodality using the peak means and standard deviations. D_A is an established and robust statistical metric for quantifying the separation between two Gaussian components in a bimodal mixture [39–41]. In brief, it provides a continuous and interpretable measure of how well two distributions are resolved within a dataset. It is calculated from the difference between the means and standard deviations of the two fitted Gaussian distributions, according to:

$$D_A = \frac{|\mu_1 - \mu_2|}{\sqrt{0.5(\sigma_1^2 + \sigma_2^2)}} \qquad \text{(Equation 3)}$$

Here, μ_1 and μ_2 represent the means, and σ_1 and σ_2 represent the standard deviations of the two components in the bimodal distribution. A D_A-value above 2 indicates that the two peaks are sufficiently and distinctly separated, with larger values corresponding to stronger bimodality. Conversely, when the two peaks share identical

means, the D_A approaches zero. Thus, D_A provides a quantitative measure to compare the degree of bimodality in pore size distributions across different supraparticles.

The mean values (μ_1 and μ_2) and standard deviations (σ_1 and σ_2) of the deconvoluted peaks, summarized in Supplementary Table T1, were used to calculate D_A-values for each supraparticle pore size distribution according to Equation 3. Then, these D_A were plotted against the sizes of the constituent nanoparticles and are shown in Figure 8 (black color). As observed in the figure, none of the supraparticles exhibit a D_A greater than 2, indicating that the two underlying distributions are not fully distinct in any case. This observation is visually evident in the MIP pore size distributions as well, where the intra- and inter-supraparticle pore peaks overlap substantially for all four samples. Moreover, the D_A-values show a decreasing trend with increasing constituent nanoparticle size. The D_A for supra-A, supra-B, supra-C, and supra–D are 1.28, 1.17, 1.10, and 1.08, respectively. These results quantitatively demonstrate that the extent of bimodality of the MIP pore size distribution of supraparticles decreases as the size of the constituent nanoparticles increases. This finding supports our expectation and visual observations that the degree of bimodality in the MIP pore size distribution is governed by the shape of the supraparticles.

To further validate the observations obtained from D_A-values, we employed the second test statistic, the so-called bimodality peak separation (S) [42]. This parameter quantifies the distance between two peaks in a bimodal distribution:

$$S = \frac{|\mu_1 - \mu_2|}{2\sigma_1 + 2\sigma_2} \qquad \text{(Equation 3)}$$

When the two Gaussian functions are completely distinct, the S-value is larger than 1. As in case of D_A, the S-values were calculated for the MIP pore size distributions of all supraparticles and plotted against the sizes of their constituent nanoparticles (Figure 8, red color). Similar to the trend observed with D_A (black color), also the S-value (red color) decreases with the size of the constituent nanoparticles. This indicates that the peaks are comparatively more distinct and better resolved when smaller nanoparticles are used.

Taken together, the results from D_A and peak separation analyses via the S-value quantitatively confirm that the bimodality of the MIP pore size distribution decreases with increasing size of the constituent nanoparticles.

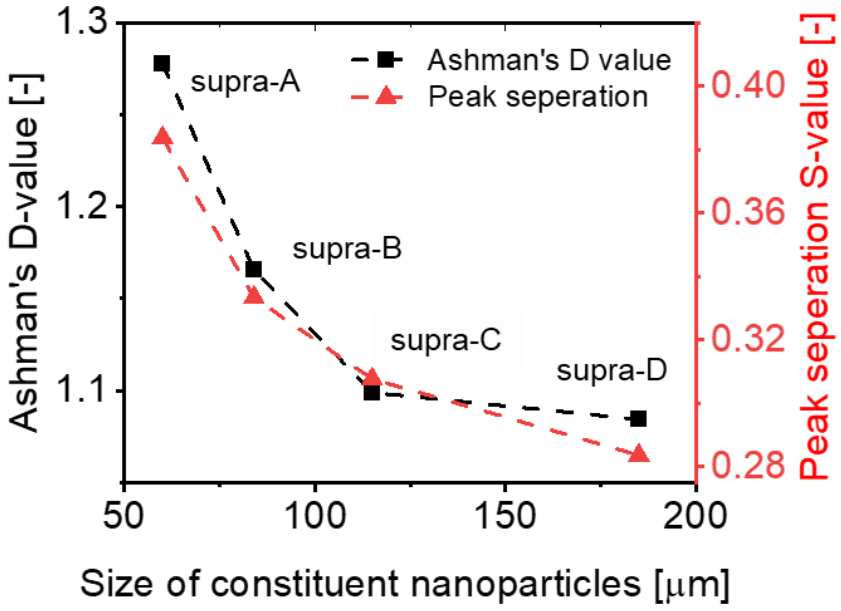

***Figure 8**: Dependence of D_A-values (black color and left axis) and values for the peak separation S (red color and right axis) of supraparticle pore size distributions on the size of the constituent nanoparticles (dashed lines are provided as a guide-to-the-eye).*

c) Correlation

So far, we have quantified both the shape of the supraparticles (via the circularity) and the extent of bimodality (via D_A and S-value) in the MIP pore size distribution and correlated it with the size of the constituent nanoparticles. In the following, the quantitative relationship between shape and extent of bimodality will be explored. Figure 9 illustrates the correlation between D_A and supraparticle circularity. First, a sharp increase in circularity is observed from 0.33 to 0.81 when D_A rises from 1.08 to 1.10. Beyond this point, the slope is clearly reduced, and the circularity shows only a very slight improvement with increasing D_A. The pronounced increase in circularity between D_A-values of 1.08 and 1.10 suggests that, for spray-dried Si/C secondary particles, a critical D_A threshold exists within this range (shaded green in Figure 9), beyond which well-defined spherical supraparticles are formed. Below the threshold, the spray-dried structures remain irregular, consisting of randomly shaped agglomerates. The slight improvement in circularity that is observed beyond the threshold D_A is attributed to roughness and minor defect variations on the supraparticle surface. A similar trend is evident in the correlation between supraparticle circularity, and the S-values derived from the MIP pore size distributions, as presented in Supplementary Figure S3. This trend supports the observation from Section 3.2.2 that

supraparticles become more spherical as the extent of bimodality of their MIP pore size distribution increases. By understanding this correlation and recognizing that the sphericity threshold for the studied samples corresponds to a D_A-value above 1.1, the shape of Si/C supraparticles can be reliably estimated from their MIP pore size distributions.

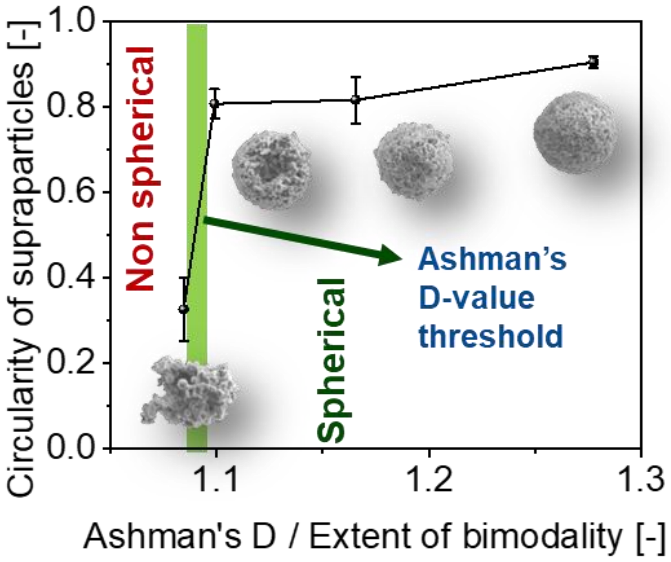

***Figure 9**: Correlation between features of the MIP pore size distribution expressed via D_A and the supraparticle shape via circularity.*

Having established a correlation between the extent of bimodality in the MIP pore size distribution and the shape (sphericity) of Si/C supraparticles produced via spray-drying, it can be concluded that MIP is a suitable technique for quality control of spray-dried supraparticles. MIP offers multiple advantages compared to conventional characterization methods. As mentioned before, the primary characteristics relevant to supraparticles are size and structural features such as shape, surface roughness and porosity, with different applications requiring supraparticles of tailored dimensions, degrees of sphericity, and porosity.

While the size of supraparticles can be conveniently determined on the ensemble level, at least as an equivalent diameter, using techniques such as AC and dynamic light scattering, comprehensive quality control should also account for shape- and pore-related characteristics. For direct visualization of particle morphology, SEM remains the most informative technique. It provides high-resolution images of individual supraparticles, revealing their exact shapes and surface features. However, obtaining

statistically meaningful conclusions from SEM data requires imaging many different particles, which makes the process time-consuming, labor-intensive, and costly, particularly when a separate porosity characterization is performed alongside imaging. MIP, by contrast, provides ensemble-averaged information and offers simultaneous insight into both porosity and supraparticle sphericity. After initial calibration, MIP is relatively rapid, scalable, and cost-effective, making it well suited for routine quality control. Although MIP does not resolve the exact particle morphology, as SEM does, it reliably quantifies how spherical or non-spherical the particles are, which is typically sufficient for spray-dried supraparticles that predominantly form near-spherical structures. The combination of structural information, statistical robustness, and measurement throughput positions MIP as a practical and efficient characterization tool within industrial workflows. A short discussion on the limitation of the developed shape-estimation method that reflects the limitations of MIP in a sense that supraparticles have to be sufficiently porous that mercury can be intruded is provided in the Supplementary Section 5.

4. Conclusions

In this study, we developed and validated a novel methodology for estimating supraparticle shape based on MIP. We first demonstrated the characteristic two-stage intrusion profile of supraparticles. To analyze these contributions in more detail, the MIP-derived pore size distributions were deconvoluted into Gaussian components with high fitting reliability ($R^2 > 0.95$). The extracted intra-supraparticle peaks were then compared with the pore size distributions of the constituent nanoparticles, and strong agreement was observed in terms of size regime and peak-shifting trends, confirming the physical validity of the deconvolution approach. A slight rightward shift of the intra-supraparticle peaks relative to the nanoparticle distributions was also consistently observed, attributable to the greater structural rigidity of supraparticles during MIP.

We then explored how the pore size distributions reflect supraparticle shape. In supraparticles of different sizes prepared from the same batch of nanoparticles, the intra-supraparticle peak remained constant, whereas the inter-supraparticle peak shifted with supraparticle size. At the same time, the overall bimodality decreased as supraparticles became smaller and more irregular in shape, as confirmed by SEM. In a complementary experiment, supraparticles of comparable size but varying shapes

were synthesized by changing the size of the feed nanoparticles. Circularity analysis from SEM images revealed progressively irregular morphologies, while MIP showed a corresponding reduction in the extent of bimodality.

To quantify this relationship, the degree of bimodality was evaluated using Ashman's D_A and peak separation (S-value), both derived from the deconvoluted pore size distributions. The statistical analyses showed that supraparticles with higher circularity values consistently exhibited stronger bimodality in their pore size distributions, whereas irregular particles showed reduced bimodality or greater overlap of peaks. This correlation provides direct evidence that the supraparticle shape can be inferred from the extent of bimodality in MIP pore size distributions.

Compared with conventional imaging methods, MIP offers distinct advantages as a quality control technique for large-scale production. It provides ensemble-averaged information, simultaneously reports porosity and shape, and is rapid, cost-effective, and statistically reliable. While SEM offers detailed visualization, it is labor-intensive and limited in statistical significance, making MIP a more practical choice for quality control. The limitations of the method are also clear. Because MIP cannot reliably resolve pores of extremely low sizes, intra-supraparticle pores cannot be characterized in systems composed of very small nanoparticles (< 10 – 20 nm). However, for supraparticles composed of nanoparticles larger than ~30 nm, as in the case of Si/C systems studied here, the methodology is robust and reliable.

This work establishes MIP as a powerful and scalable tool for concurrent characterization of supraparticle porosity and shape. Beyond advancing the fundamental understanding of supraparticle structure, the method provides a practical pathway for process optimization and quality control in the large-scale production of supraparticles for energy storage, catalysis, and related applications. Looking ahead, extending this approach to supraparticles built from smaller nanoparticles (<20 nm) will require integrating complementary techniques with higher resolution for small pores, such as nitrogen adsorption porosimetry, thereby broadening the applicability of shape estimation methodologies to a wider class of nanostructured supraparticles. Furthermore, future studies should also explore the applicability of this method to supraparticles formed from anisotropic feed materials—such as nanorods, nanotubes,

or plate-like particles—to evaluate how feed particle anisotropy influences pore structure and the resulting MIP-based shape estimation.

Acknowledgements

This research was financially supported by the Federal Ministry of Economic Affairs and Climate Action, Germany (funding code 03EI3027A), for which the authors are sincerely grateful. The authors also wish to thank Mr. Simon Heckenbach for his assistance during the experiments, and the Interdisciplinary Center for Analytics on the Nanoscale (ICAN) for providing analytical measurement support. The authors also acknowledge the MAT4HY.NRW Consortium for cooperative support.)

Data availability

All the data acquired for this study is openly available on Nomad.

Declaration of AI-assisted technologies in the writing process

During the preparation of this manuscript, the authors utilized the AI tool ChatGPT 5.2 from OpenAI to enhance the clarity and readability of the text. Following its use, the authors carefully reviewed and revised the content as necessary and bear full responsibility for the final version of the published article.

References

[1] S. Wintzheimer, T. Granath, M. Oppmann, T. Kister, T. Thai, T. Kraus, N. Vogel, K. Mandel, Supraparticles: Functionality from Uniform Structural Motifs, ACS Nano 12 (2018) 5093–5120. https://doi.org/10.1021/acsnano.8b00873.

[2] J. Guo, W. Yang, C. Wang, Magnetic colloidal supraparticles: design, fabrication and biomedical applications, Adv. Mater. 25 (2013) 5196–5214. https://doi.org/10.1002/adma.201301896.

[3] J. Guo, B.L. Tardy, A.J. Christofferson, Y. Dai, J.J. Richardson, W. Zhu, M. Hu, Y. Ju, J. Cui, R.R. Dagastine, I. Yarovsky, F. Caruso, Modular assembly of superstructures from polyphenol-functionalized building blocks, Nat. Nanotechnol. 11 (2016) 1105–1111. https://doi.org/10.1038/nnano.2016.172.

[4] S. Ulrich, C. Hirsch, L. Diener, P. Wick, R.M. Rossi, M.B. Bannwarth, L.F. Boesel, Preparation of ellipsoid-shaped supraparticles with modular compositions and investigation of shape-dependent cell-uptake, RSC Adv. 6 (2016) 89028–89039. https://doi.org/10.1039/C6RA19861A.

[5] Y. Xia, Z. Tang, Monodisperse inorganic supraparticles: formation mechanism, properties and applications, Chem. Commun. (Camb) (2012). https://doi.org/10.1039/c2cc31354e.

[6] A. Amin, M. Loewenich, S.O. Kilian, T. Wassmer, S. Bade, J. Lyubina, H. Wiggers, F. Özcan, D. Segets, One-Step Non-Reactive Spray Drying Approach to Produce Silicon/Carbon Composite-Based Hierarchically Structured Supraparticles for Lithium-Ion Battery Anodes, J. Electrochem. Soc. 170 (2023) 20523. https://doi.org/10.1149/1945-7111/acb66b.

[7] A. Amin, M. Loewenich, L. Grebener, M. Hammad, S. Heckenbach, M.-A. Kräenbring, A.S. Odungat, A.H. Ladole, T.B. Nguyen, D. Schwabenland, H.K. Salim, H. Wiggers, D. Segets, F. Özcan, Impact of Supraparticle Sizes and Morphology on Interparticle Spacing, Slurry Rheology, Coating Density, and Electrochemical Performance in Si/C Anodes for Li-Ion Batteries, ACS Appl. Energy Mater. 8 (2025) 2050–2063. https://doi.org/10.1021/acsaem.4c02578.

[8] Y.-S. Ko, Y.H. Joe, M. Seo, K. Lim, J. Hwang, K. Woo, Prompt and synergistic antibacterial activity of silver nanoparticle-decorated silica hybrid particles on air filtration, J. Mater. Chem. B 2 (2014) 6714–6722. https://doi.org/10.1039/C4TB01068J.

[9] A. Uchida, Y. Kitayama, E. Takano, T. Ooya, T. Takeuchi, Supraparticles comprised of molecularly imprinted nanoparticles and modified gold

nanoparticles as a nanosensor platform, RSC Adv. 3 (2013) 25306. https://doi.org/10.1039/C3RA43660H.

[10] G. Ro, D.K. Hwang, Y. Kim, Hydrogen generation using Pt/Ni bimetallic nanoparticles supported on Fe3O4@SiO2@TiO2 multi-shell microspheres, Journal of Industrial and Engineering Chemistry 79 (2019) 364–369. https://doi.org/10.1016/j.jiec.2019.07.011.

[11] K. Hou, J. Han, Z. Tang, Formation of Supraparticles and Their Application in Catalysis, ACS Materials Lett. 2 (2020) 95–106. https://doi.org/10.1021/acsmaterialslett.9b00446.

[12] J.W. Yoo, K. Zhang, V. Patil, J.T. Lee, D.-W. Jung, L.S. Pu, W. Oh, W.-S. Yoon, J.H. Park, G.-R. Yi, Porous supraparticles of LiFePO 4 nanorods with carbon for high rate Li-ion batteries, mat express 8 (2018) 316–324. https://doi.org/10.1166/mex.2018.1443.

[13] Z. Cao, X. Chen, L. Xing, Y. Liao, M. Xu, X. Li, X. Liu, W. Li, Nano-MnO2@TiO2 microspheres: A novel structure and excellent performance as anode of lithium-ion batteries, Journal of Power Sources 379 (2018) 174–181. https://doi.org/10.1016/j.jpowsour.2018.01.058.

[14] X. Zhou, Z. Li, X. Deng, B. Yan, Z. Wang, X. Chen, S. Huang, High performance perovskite solar cells using Cu9S5 supraparticles incorporated hole transport layers, Nanotechnology 30 (2019) 445401. https://doi.org/10.1088/1361-6528/ab3604.

[15] C.K. Chan, H. Peng, G. Liu, K. McIlwrath, X.F. Zhang, R.A. Huggins, Y. Cui, High-performance lithium battery anodes using silicon nanowires, Nat. Nanotechnol. 3 (2008) 31–35. https://doi.org/10.1038/nnano.2007.411.

[16] H. Wu, G. Yu, L. Pan, N. Liu, M.T. McDowell, Z. Bao, Y. Cui, Stable Li-ion battery anodes by in-situ polymerization of conducting hydrogel to conformally coat silicon nanoparticles, Nat. Commun. 4 (2013) 1943. https://doi.org/10.1038/ncomms2941.

[17] W. Xu, S.S.S. Vegunta, J.C. Flake, Surface-modified silicon nanowire anodes for lithium-ion batteries, Journal of Power Sources 196 (2011) 8583–8589. https://doi.org/10.1016/j.jpowsour.2011.05.059.

[18] T. Shao, J. Liu, L. Gan, Z. Gong, M. Long, Yolk-shell Si@void@C composite with Chito-oligosaccharide as a C–N precursor for high capacity anode in lithium-ion batteries, Journal of Physics and Chemistry of Solids 152 (2021) 109965. https://doi.org/10.1016/j.jpcs.2021.109965.

[19] J. Guo, X. Chen, C. Wang, Carbon scaffold structured silicon anodes for lithium-ion batteries, J. Mater. Chem. 20 (2010) 5035. https://doi.org/10.1039/C0JM00215A.

[20] N. Liu, Z. Lu, J. Zhao, M.T. McDowell, H.-W. Lee, W. Zhao, Y. Cui, A pomegranate-inspired nanoscale design for large-volume-change lithium battery anodes, Nat. Nanotechnol. 9 (2014) 187–192. https://doi.org/10.1038/nnano.2014.6.

[21] J. Lyubina, 2021. Phase transformations and hysteresis in Si-based anode materials. Applied Physics Letters 118, 090501. https://doi.org/10.1063/5.0031416.

[22] H. Jia, J. Zheng, J. Song, L. Luo, R. Yi, L. Estevez, W. Zhao, R. Patel, X. Li, J.-G. Zhang, A novel approach to synthesize micrometer-sized porous silicon as a high performance anode for lithium-ion batteries, Nano Energy 50 (2018) 589–597. https://doi.org/10.1016/j.nanoen.2018.05.048.

[23] S.K. Kim, C. Kim, H. Chang, H.D. Jang, Preparation of Silicon-Carbon-Graphene Composites and their Application to Lithium Ion Secondary Battery, Aerosol Air Qual. Res. 22 (2022) 220009. https://doi.org/10.4209/aaqr.220009.

[24] S. Müllner, T. Held, A. Schmidt-Rodenkirchen, T. Gerdes, C. Roth, Reactive Spray Drying as a One-Step Synthesis Approach towards Si/rGO Anode Materials for Lithium-Ion Batteries, J. Electrochem. Soc. 168 (2021) 120545. https://doi.org/10.1149/1945-7111/ac429d.

[25] Z. Yan, J. Guo, High-performance silicon-carbon anode material via aerosol spray drying and magnesiothermic reduction, Nano Energy 63 (2019) 103845. https://doi.org/10.1016/j.nanoen.2019.06.041.

[26] U. Sultan, A. Götz, C. Schlumberger, D. Drobek, G. Bleyer, T. Walter, E. Löwer, U.A. Peuker, M. Thommes, E. Spiecker, B. Apeleo Zubiri, A. Inayat, N. Vogel, From Meso to Macro: Controlling Hierarchical Porosity in Supraparticle Powders, Small 19 (2023) e2300241. https://doi.org/10.1002/smll.202300241.

[27] W. Liu, M. Kappl, H.-J. Butt, Tuning the Porosity of Supraparticles, ACS Nano 13 (2019) 13949–13956. https://doi.org/10.1021/acsnano.9b05673.

[28] H. Orthner, H. Wiggers, M. Loewenich, S. Kilian, S. Bade, J. Lyubina, Direct gas phase synthesis of amorphous Si/C nanoparticles as anode material for lithium ion battery, Journal of Alloys and Compounds 870 (2021) 159315. https://doi.org/10.1016/j.jallcom.2021.159315.

[29] Z. Kang, Q. Li, J. Zhang, P. Cheng, Effects of gas liquid ratio on the atomization characteristics of gas-liquid swirl coaxial injectors, Acta Astronautica 146 (2018) 24–32. https://doi.org/10.1016/j.actaastro.2018.02.026.

[30] M. Hammad, S. Angel, A.K. Al-Kamal, A. Asghar, A. Said Amin, M.-A. Kräenbring, H.T. Wiedemann, V. Vinayakumar, M. Yusuf Ali, P. Fortugno, C.

Kim, T.C. Schmidt, C.W. Kay, C. Schulz, D. Segets, H. Wiggers, Synthesis of novel LaCoO3/graphene catalysts as highly efficient peroxymonosulfate activator for the degradation of organic pollutants, Chemical Engineering Journal 454 (2023) 139900. https://doi.org/10.1016/j.cej.2022.139900.

[31] M. Hammad, A. Amin, A. Asghar, O. Anwar, S. Salamon, J. Landers, M.-A. Kräenbring, A. Jain, S. Hardt, H. Wiggers, T.C. Schmidt, H. Wende, C. Schulz, D. Segets, Polyacrylic acid functionalized superparamagnetic iron-oxide supraparticles for highly efficient adsorption and removal of contaminants from water, Journal of Water Process Engineering 66 (2024) 106025. https://doi.org/10.1016/j.jwpe.2024.106025.

[32] A.S. Amin, R. Martinez-Hincapié, A.R. Khan, A. Olean-Oliveira, A.S. Odungat, A. Gurowski, A. Jain, L. Grebener, A. Rezvani, M. Hammad, T. Lange, F. Özcan, V. Čolić, D. Segets, The impact of ink processing on key characteristics of platinum detachment and pore structure to optimize fuel cell performance, International Journal of Hydrogen Energy 144 (2025) 1240–1256. https://doi.org/10.1016/j.ijhydene.2025.04.450.

[33] H. Giesche, Mercury Porosimetry: A General (Practical) Overview, Part & Part Syst Charact 23 (2006) 9–19. https://doi.org/10.1002/ppsc.200601009.

[34] L. Grebener, A.S. Odungat, Y. Zhu, O. Pasdag, I. Radev, E. Nürenberg, A. Kubina, V. Peinecke, S. Kohsakowski, D. Segets, F. Özcan, Investigation of fuel cell catalyst dispersion formulations for indirect roll-to-roll fabrication of catalyst coated membranes for proton exchange membrane fuel cells, Journal of Power Sources 635 (2025) 236457. https://doi.org/10.1016/j.jpowsour.2025.236457.

[35] V. Vinayakumar, T. Wagner, C. Marcks, J. Johny, G. Wartner, A. Lim, M.F. Tesch, I. Spanos, A. Ghafari, A. Jain, O. Prymak, I. Sanjuán, A.S. Odungat, O.

Anwar, M. Chatwani, A. Jose, V. Chanda, A. Knop-Gericke, C. Andronescu, A.K. Mechler, N. Wöhrl, D. Segets, Ni-Co-O anodes for the alkaline oxygen evolution reaction: Multistage electrode optimization and plasma-assisted activity enhancement enabled by a coherent workflow, Chemical Engineering Journal (2025) 167169. https://doi.org/10.1016/j.cej.2025.167169.

[36] J. Zhao, H. Liu, X. Li, Structure, Property, and Performance of Catalyst Layers in Proton Exchange Membrane Fuel Cells, Electrochem. Energ. Rev. 6 (2023) 13. https://doi.org/10.1007/s41918-022-00175-1.

[37] A.S. Odungat, L. Grebener, O. Pasdag, T.B. Nguyen, Y. Zhu, S. Kohsakowski, I. Radev, F. Özcan, D. Segets, 2025. A Multiscale Pore Analysis Method for Polymer Electrolyte Membrane Fuel Cell Catalyst Layers Validated and Exemplified by Correlating Microstructure with Production Process Parameters. Adv Energy and Sustain Res, 2500043. https://doi.org/10.1002/aesr.202500043.

[38] J. Wang, J. Schwenger, A. Ströbel, P. Feldner, P. Herre, S. Romeis, W. Peukert, B. Merle, N. Vogel, Mechanics of colloidal supraparticles under compression, Sci. Adv. 7 (2021) eabj0954. https://doi.org/10.1126/sciadv.abj0954.

[39] K.M. Ashman, C.M. Bird, S.E. Zepf, Detecting Bimodality in Astronomical Datasets (1994). https://doi.org/10.48550/arXiv.astro-ph/9408030.

[40] S. Shi, D. Guo, J. Luo, Enhanced phase and amplitude image contrasts of polymers in bimodal atomic force microscopy, RSC Adv. 7 (2017) 11768–11776. https://doi.org/10.1039/C6RA27902C.

[41] S. Shi, D. Guo, J. Luo, Interfacial interaction and enhanced image contrasts in higher mode and bimodal mode atomic force microscopy, RSC Adv. 7 (2017) 55121–55130. https://doi.org/10.1039/C7RA11635G.

[42] C. Zhang, B.E. Mapes, B.J. Soden, Bimodality in tropical water vapour, Quart J Royal Meteoro Soc 129 (2003) 2847–2866. https://doi.org/10.1256/qj.02.166.

[43] M. Hammad, B. Toplak, A. Amin, M.-A. Kräenbring, A.S. Odungat, M.-A. Sheikh, A. Jain, A.S. Amin, R. Meckenstock, T.B. Nguyen, K.Y. Muhammad, A. Hamdan, S. Angel, M. Farle, U.-P. Apfel, H. Wiggers, D. Segets, Supraparticle Assembly of La0.8Sr0.2CoO3 Nanoparticles for Enhanced Lattice Oxygen Oxidation in Alkaline Electrolysis, ACS Appl. Mater. Interfaces 17 (2025) 53413–53426. https://doi.org/10.1021/acsami.5c11289.

[44] S.P. Rigby, Uses of Gas Sorption and Mercury Porosimetry Methods in Studies of Heritage Materials, Heritage 8 (2025) 132. https://doi.org/10.3390/heritage8040132.

[45] J. van Brakel, S. Modrý, M. Svatá, Mercury porosimetry: state of the art, Powder Technology 29 (1981) 1–12. https://doi.org/10.1016/0032-5910(81)85001-2.

Supplementary Information

Mercury intrusion porosimetry as a quantitative tool for the shape estimation of supraparticles generated via spray-drying

*Ahammed Suhail Odungat[1, †], Adil Amin[1, †], Moritz Loewenich[2], Blaž Toplak[1], Mena-Alexander Kräenbring[1], Mohaned Hammad[1], Hartmut Wiggers[2,3], Doris Segets[1,3], Fatih Özcan[1, 3, *]*

[1]Institute for Energy and Materials Processes – Particle Science and Technology (EMPI – PST), University of Duisburg-Essen (UDE), Germany

[2]Institute for Energy and Materials Processes − Reactive Fluids (EMPI – RF), University of Duisburg-Essen (UDE), Germany

[3]Center for Nanointegration Duisburg-Essen (CENIDE), University of Duisburg-Essen (UDE), Germany

Corresponding Author

[*]Email: fatih.oezcan@uni-due.de

[†]*These authors contributed equally to this work*

1. TEM images of nanoparticles

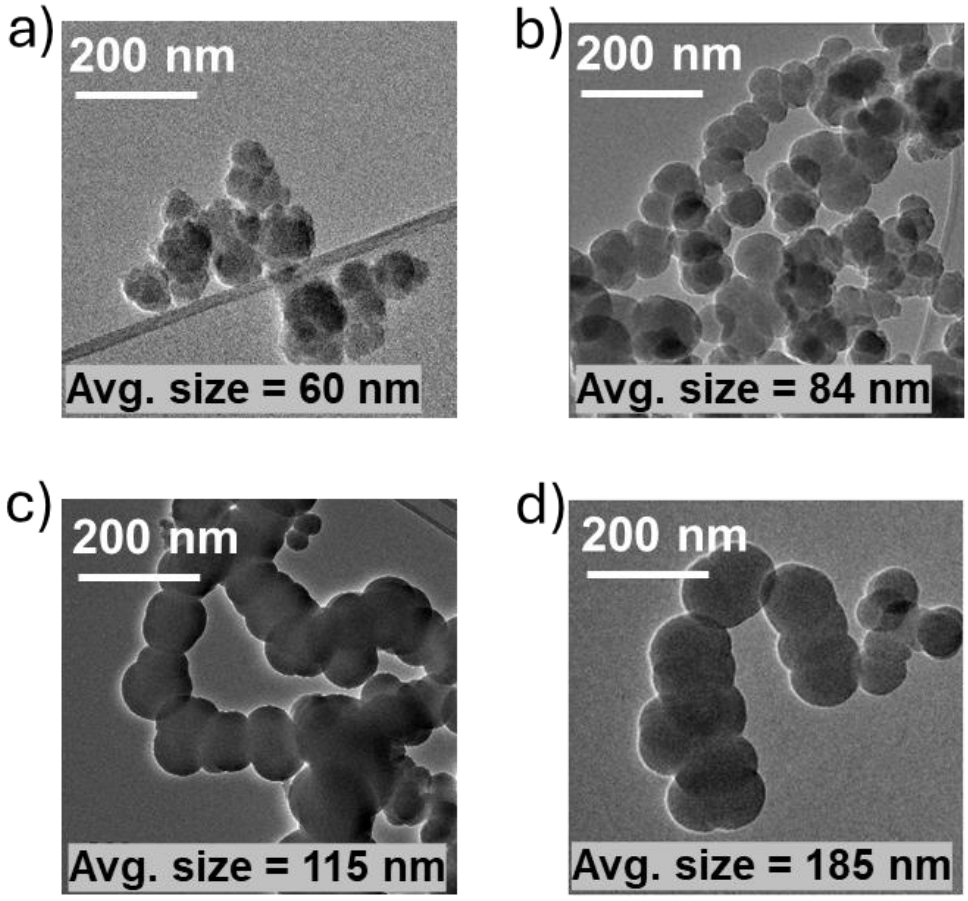

***Supplementary Figure S1**: TEM images of nanoparticles used to prepare (a) supra-A, (b) supra-B, (c) supra-C and (d) supra-D*

2. Supraparticle size analysis

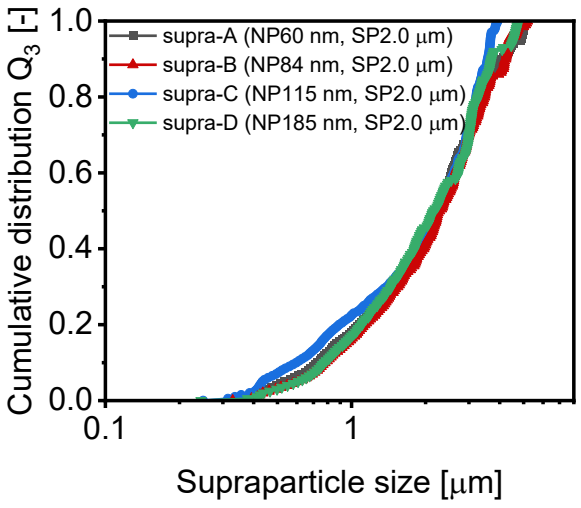

***Supplementary Figure S2**: Particle size distribution of supraparticles analyzed using AC*

3. MIP pore size distribution deconvolution

	μ_1 (µm)	μ_2 (µm)	σ_1 (µm)	σ_2 (µm)
supra-A	0.84	0.28	0.61	0.11
supra-B	0.62	0.26	0.42	0.12
supra-C	1.06	0.34	0.88	0.29
supra-D	1.06	0.47	0.68	0.36

Supplementary Table T1*: Mean pore diameters and standard deviations of inter-supraparticle pores (μ_1 and σ_1) and intra-supraparticle pores (μ_2 and σ_2) obtained by deconvoluting MIP pore size distributions.*

4. Supraparticle shape – peak separation value correlation

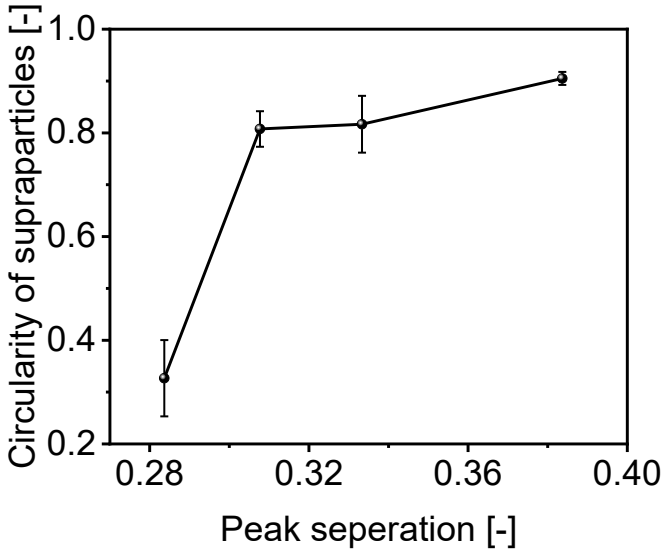

Supplementary Figure S3*: Correlation between features of the MIP pore size distribution expressed via S-value and the supraparticle shape via circularity.*

5. Limitations of MIP-shape estimation method

5.1. Preparation of LSCO supraparticles

LSCO nanoparticles were synthesized via spray-flame synthesis following the protocol developed by Hammad et al [30]. To prepare the spray-drying mixture, 0.9 g of LSCO nanoparticles was dispersed in 300 mL of ultrapure water together with 4.5 mL of a 5 wt% Sustainion® XA-9 solution in ethanol from Dioxide Materials. The mixture was

sonicated in an ice bath, following the procedure described in a previous study [31], to ensure homogeneous dispersion. The resulting suspension was subjected to spray-drying using the same procedure as outlined in Section 2.1a for Si/C supraparticles. The only difference was that the GLR was fixed at 3.5k.

5.2. MIP analysis of LSCO supraparticles

The limitation of MIP as a shape estimation method must also be investigated. For this purpose, supraparticles synthesized from LSCO nanoparticles were selected. LSCO nanoparticles are well known for their high surface area and enhanced oxygen evolution reaction (OER) performance in alkaline electrolysis. Hammad et al. demonstrated that replacing LSCO nanoparticles with spray-dried LSCO supraparticles led to significant improvements in OER performance [1]. Using LSCO supraparticles to test the limitation of our shape estimation by MIP offers an additional advantage. In the main manuscript, the supraparticles analyzed were primarily ~2 µm in size and composed of Si/C nanoparticles with mean primary particle sizes ranging from 60 to 185 nm. By contrast, the LSCO nanoparticles synthesized via spray-flame synthesis have a much smaller average primary particle diameter of 8.2 nm, as determined from TEM images (Supplementary Figure S4a). Evaluating LSCO supraparticles therefore enables us to assess how the method performs when the constituent nanoparticles are significantly smaller relative to the overall supraparticle size.

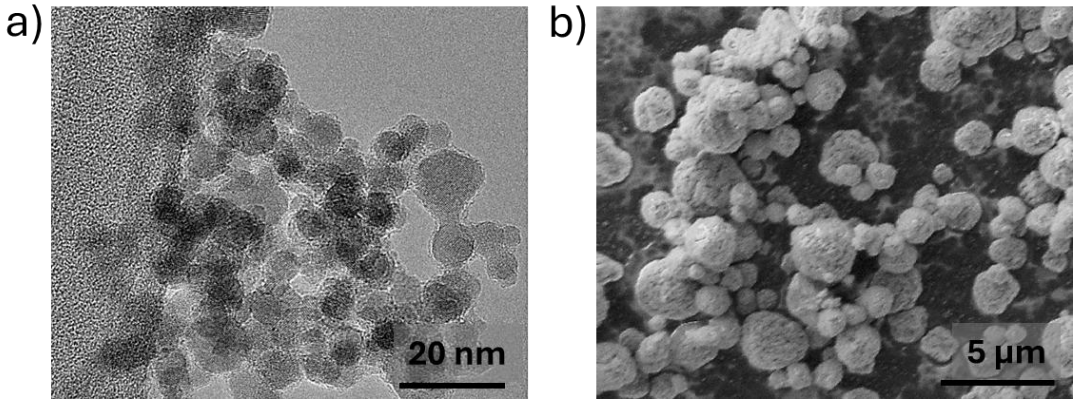

Supplementary Figure S4*: Characterization of LSCO nanoparticles and supraparticles. (a) TEM image of LSCO nanoparticles; b) SEM image of LSCO supraparticles.*

LSCO supraparticles were synthesized by spray-drying by keeping the GLR at 3.5K so that the resulting supraparticles had an average size of ~2.0 µm (Supplementary Figure S4b). SEM imaging confirmed that the supraparticles were predominantly

spherical in shape. The MIP pore size distribution of LSCO supraparticles (Supplementary Figure S5a) reveals two distinct features, a pronounced peak centered at ~0.5 μm corresponding to inter-supraparticle pores, and a small elevation at pore sizes below 0.02 μm, associated with intra-supraparticle pores. This behavior contrasts with the Si/C supraparticles, which exhibited two overlapping but well-defined peaks. In LSCO supraparticles, the inter-supraparticle pores are clearly represented by a defined peak, whereas the intra-supraparticle contribution appears only as a minor elevation rather than a distinct peak.

A similar trend is observed in the MIP pore size distributions of the LSCO nanoparticles (Supplementary Figure S5b), where only minor peaks appear in the sub 0.02 μm range with very low intrusion volumes. This limitation can be attributed to the resolution of the MIP technique. It is well established that MIP is not accurate for characterizing pores of low sizes due to the involvement of extremely high pressure during the measurement [2,3]. Given that the LSCO nanoparticles used here have an average size of 8.2 nm, the voids between them in the supraparticles are expected to fall within the same dimension range, which explains the absence of a clear intra-supraparticle peak in the MIP data.

Therefore, MIP cannot be reliably used to analyze the intra-supraparticle pores of LSCO supraparticles. As a result, the MIP-based shape deduction method is not applicable to supraparticles composed of nanoparticles smaller than ~10–20 nm. This limitation arises from the inherent resolution constraints of the MIP technique itself. Nevertheless, the method remains highly effective for Si/C supraparticles and other systems in which the constituent nanoparticles have sizes greater than ~30 nm, where intra-supraparticle pores fall within the measurable range of MIP.

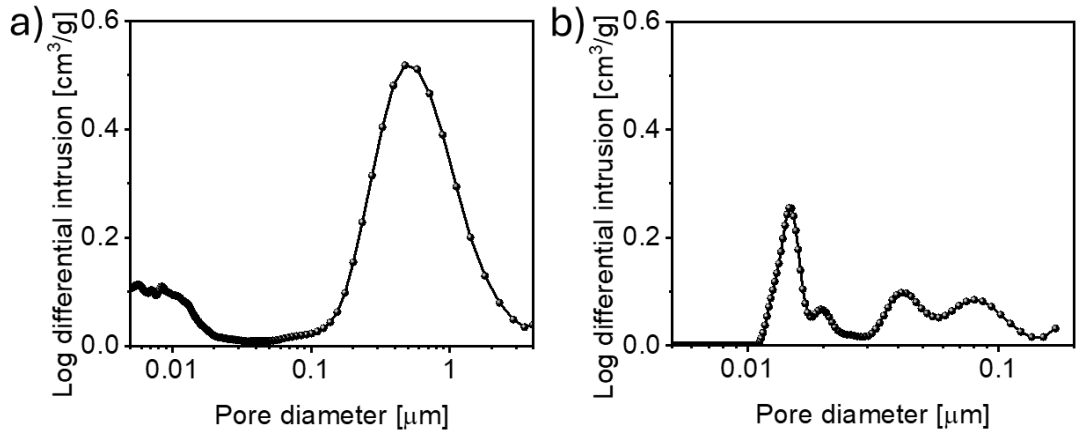

Supplementary Figure S5*: Structural characterization of LSCO supraparticles and nanoparticles. MIP pores size distribution of (a) LSCO supraparticles and (b) LSCO nanoparticles.*

References

[1] M. Hammad, B. Toplak, A. Amin, M.-A. Kräenbring, A.S. Odungat, M.-A. Sheikh, A. Jain, A.S. Amin, R. Meckenstock, T.B. Nguyen, K.Y. Muhammad, A. Hamdan, S. Angel, M. Farle, U.-P. Apfel, H. Wiggers, D. Segets, Supraparticle Assembly of La0.8Sr0.2CoO3 Nanoparticles for Enhanced Lattice Oxygen Oxidation in Alkaline Electrolysis, ACS Appl. Mater. Interfaces 17 (2025) 53413–53426. https://doi.org/10.1021/acsami.5c11289.

[2] J. van Brakel, S. Modrý, M. Svatá, Mercury porosimetry: state of the art, Powder Technology 29 (1981) 1–12. https://doi.org/10.1016/0032-5910(81)85001-2.

[3] S.P. Rigby, Uses of Gas Sorption and Mercury Porosimetry Methods in Studies of Heritage Materials, Heritage 8 (2025) 132. https://doi.org/10.3390/heritage8040132.